Theor Chem Acc (2007) 117:943–956
DOI 10.1007/s00214-006-0212-3

REGULAR ARTICLE

Recent advances in molecular photoionization by density functional theory based approaches

M. Stener · D. Toffoli · G. Fronzoni · P. Decleva

Received: 21 June 2006 / Accepted: 13 October 2006 / Published online: 13 December 2006
© Springer-Verlag 2006

Abstract The most recent advances in the theoretical description of molecular photoionization by means of the Density Functional Theory with B-splines basis functions is reviewed. From the methodological point of view, the formalism of the Time Dependent Density Functional Theory applied to molecular continuum is considered, with a new implementation based on a non-iterative algorithm. Also, applications of the Kohn–Sham method for the calculation of dichroism in photoionization of chiral molecules and of dynamical parameters beyond the dipole approximation are considered. The methods have proved successful to accurately reproduce experimental data and to suggest reliable assignments to observed spectral features.

Keywords Density functional theory · Photoionization · Dichroism · Non-dipolar effects · B-spline

1 Introduction

Density Functional Theory (DFT) based on the Kohn–Sham [1] (KS) scheme is nowadays widely employed to study the ground state electronic structure and the properties of large molecules. On the other hand, the theoretical description of photoionization needs the explicit calculation of the photoelectron unbound states. This task cannot be easily afforded by standard basis sets like for example gaussians or Slater Type Orbitals (STO) and a standard method has not yet consolidated in this field. In our group, we have developed new algorithms based on a non-conventional basis set consisting of B-spline functions [2]. These algorithms have been implemented at various levels of theory in computer codes and some of them have been parallelized in order to exploit modern supercomputer architectures.

In this work, we present the most recent and relevant achievements in the field of molecular photoionization obtained by employing B-spline basis function. Both methodological and applicative aspects will be considered. From the methodological point of view, we will discuss the Time Dependent DFT (TDDFT) scheme [3], which represents the state-of-the-art formalism to manage molecular excited states at the DFT level. We will illustrate our implementation of the TDDFT equations for the continuum, based on an original non-iterative algorithm, which avoids the SCF procedure typical of standard TDDFT quantum chemistry codes, usually employed, for example, to calculate dynamical (hyper)-polarizabilities [4].

The resolution of the TDDFT equations for the molecular continuum was originally implemented with an iterative algorithm employing a One Center Expansion (OCE) B-spline basis set and applied to a series of small molecules: N_2, PH_3 [5], hydrides [6,7], CO [8] and C_2H_2 [9]. Although excellent results were obtained with respect to the experiment, the original formulation suffered from essentially two problems. First, the OCE

M. Stener (✉) · D. Toffoli · G. Fronzoni · P. Decleva
Dipartimento di Scienze Chimiche, Università di Trieste,
Via L. Giorgieri 1, Trieste 34127, Italy
e-mail: Stener@Univ.trieste.it

M. Stener · D. Toffoli · G. Fronzoni · P. Decleva
Consorzio Interuniversitario Nazionale per la Scienza e Tecnologia dei Materiali, INSTM, Unità di Trieste, Trieste, Italy

M. Stener · D. Toffoli · G. Fronzoni · P. Decleva
INFM DEMOCRITOS National Simulation Center, Trieste, Italy

basis prevented the consideration of larger systems, limiting the applicability to only linear systems or molecules with very light off-center atoms like hydrides. Second, the iterative procedure in some instances showed difficulties in converging, suggesting attempts to solve the TDDFT equations with alternative algorithms avoiding the SCF process. We have recently met both goals with the new implementation of the TDDFT code with multicentric B-spline basis set and a non-iterative algorithm [10], which has been applied to several medium sized systems: CS_2 and C_6H_6 [10] and to a series of fluorine containing molecules, namely SF_6 [11], SiF_4 [12] and CF_4 [13]. These systems were chosen because experimental data are available to test the performance of the method and also because they exhibit interesting spectral features, which deserve further theoretical analysis. In the present work, we will only consider the most significant results relative to SF_6, which, however, is a good representative of the general level of accuracy of the present method.

From the applicative point of view, we have considered two peculiar photoionization effects which have become targets of recent studies, whose description have been adequately obtained with the B-spline method already at the Kohn–Sham level: namely the Circular Dichroism in Angular Distribution (CDAD) of photoelectrons from chiral molecules and the non-dipolar effects in molecular photoionization.

Circular Dichroism in Angular Distribution of photoelectrons from chiral molecules can be revealed in unoriented chiral molecules by angle-resolved photoelectron spectroscopy involving either valence or inner-shell electrons. It has been demonstrated theoretically [14,15] that dichroism effect dependent on the helicity of the circularly polarized light should be observed in the photoelectron emission even from randomly oriented chiral molecules. This effect, referred as CDAD, is governed purely by the electric dipole operator and its magnitude is therefore expected to be much stronger than the conventional circular dichroism observed in photoabsorption, which depends upon electric quadrupole or magnetic dipole operator contributions. Only recently progress in synchrotron radiation techniques has allowed the experimental measurement of the CDAD effects in rigid chiral molecules such as bromocamphor [16], camphor [17,18], and methyloxirane [19] and then on floppy molecules [20]. Efforts to perform theoretical calculations of the dichroism effect based on continuum multiple scattering (CMS-Xα) [21,22] and B-spline methods [19,23] on large organic chiral molecules have recently started. The calculation of the dichroism needs the knowledge of the continuum photoelectron wave function, therefore at present both CMS-Xα and B-spline methods are available for this task. The LCAO B-spline DFT approach does not introduce any approximation on the potential, at variance with the MS-Xα approach, therefore the quality of the DFT results is expected to be higher as well as of predictive potential. It is worth noting that the CDAD calculations are computationally very demanding, because the usual chiral molecules are rather large and nonsymmetric and therefore it is mandatory to employ a parallel version of the computer code in order to take maximum advantage of the architecture of modern supercomputers.

Experimental and theoretical work on non-dipolar effects in molecular photoionization have been very limited so far. Notably, two papers focusing on the K-shell photoionization of molecular nitrogen report contradicting experimental results [24–26]. While the first measurements gave evidence of strong nondipole effects at very low photoelectron kinetic energies [24,25], results of a recent investigation strongly contradict earlier findings [26]. In the work of Ref. [26], negligible nondipole effects are detected, even if strong near-threshold departures from the dipolar behavior are theoretically predicted for the individual $1\sigma_g^{-1}$ and $1\sigma_u^{-1}$ ionization channels.

2 Computational models

In all cases considered, the first step consists in performing a conventional quantum chemistry calculation of the ground state density of the molecule. To this end we employ the *ADF* [27,28] program, which solves the KS equations within a basis set of Slater functions. Once the ground state electron density is obtained, the KS hamiltonian matrix is calculated, employing the B-spline basis set. The KS hamiltonian includes the exchange-correlation potential, whose correct asymptotic behavior is important to gain accurate results for continuum calculations. Therefore, we have considered both LB94 [29] and in some instances the more recent SAOP [30] potentials, both of which support the Coulomb tail at large distances.

Two different strategies can be actually employed to build the molecular B-spline basis set. The most straightforward is to consider an OCE [31] with basis functions obtained as products between monodimensional radial B-splines and real spherical harmonics adapted to the molecular point group symmetry, all centered on a common origin. The OCE basis set is rather simple to be implemented and is numerically stable, but characterized by slow converge properties and therefore its use is practicable only for very small or highly symmetric molecules. A better alternative choice is a Linear

Combination of Atomic Orbitals (LCAO) basis, which is obtained supplementing the OCE set with additional B-splines centered on the off-origin nuclei positions [32]. This second alternative is more difficult to be implemented because of the need of efficient algorithms for the evaluation of matrix elements between basis functions lying on different centers, but it is more efficient since it converges more quickly than the OCE with basis set enlargement.

Once a specific B-spline basis is chosen (OCE or LCAO), occupied orbitals are then obtained as bound eigenvectors of the KS hamiltonian matrix:

$$H_{\mathrm{KS}}\varphi_i = \varepsilon_i\varphi_i \quad i = 1,\ldots,n, \tag{1}$$

while continuum photoelectron orbitals are extracted as eigenvectors with minimum modulus eigenvalue of the energy dependent matrix $\mathbf{A}^{+}\mathbf{A}$:

$$\mathbf{A}^{+}\mathbf{A}(E)c = ac, \quad \mathbf{A}(E) = \mathbf{H} - E\mathbf{S}. \tag{2}$$

In Eq. (2), **H** and **S** are the Hamiltonian and overlap matrices respectively, E is the photoelectron kinetic energy, c are the eigenvectors and a the minimum modulus eigenvalues. Eigenvectors c are then normalized according to S-matrix incoming wave boundary conditions, giving a set of partial waves $\psi_{lh}^{p\mu(-)}(r)$, which are employed to calculate the various dynamical parameters. This step completes the KS procedure and the cross section and asymmetry parameter profiles can be calculated via transition moments between occupied and continuum orbitals.

In the TDDFT formalism, the linear response of an electronic density to an external weak time–dependent electromagnetic field with frequency ω is evaluated following the original scheme of Zangwill and Soven [33]; an effective Self-Consistent Field (SCF) potential Φ^{SCF} is introduced, which consists of the external dipole potential Φ^{EXT} plus the Coulomb and exchange-correlation screening due to the redistribution of the electrons:

$$\Phi^{\mathrm{SCF}}(\bar{r},\omega) = \Phi^{\mathrm{EXT}}(\bar{r},\omega) + \int \frac{\delta n(\bar{r}',\omega)\,\mathrm{d}\bar{r}'}{|\bar{r}-\bar{r}'|} + \left.\frac{\partial V_{XC}}{\partial n}\right|_{n(\bar{r})} \delta n(\bar{r},\omega). \tag{3}$$

In Eq. (3), $\delta n(\bar{r},\omega)$ is the induced density and the Adiabatic Local Density Approximation (ALDA) [34] to the exchange-correlation kernel has been introduced. In turn, the induced density is obtained from the KS (noninteracting) dielectric susceptibility (χ) and the SCF potential:

$$\delta n(\bar{r},\omega) = \int \chi(\bar{r},\bar{r}',\omega)\,\Phi^{\mathrm{SCF}}(\bar{r}',\omega)\,\mathrm{d}\bar{r}'. \tag{4}$$

Substitution of (4) in (3) gives the integral equation:

$$\Phi^{\mathrm{SCF}}(\bar{r},\omega) = \Phi^{\mathrm{EXT}}(\bar{r},\omega) + \int\int K(\bar{r},\bar{r}')\chi(\bar{r}',\bar{r}'',\omega) \times \Phi^{\mathrm{SCF}}(\bar{r}'',\omega)\,\mathrm{d}\bar{r}'\mathrm{d}\bar{r}'' \tag{5}$$

where in (5) K represents the coulomb and the ALDA exchange-correlation kernel:

$$K(\bar{r},\bar{r}') = \frac{1}{|\bar{r}-\bar{r}'|} + \delta(\bar{r}-\bar{r}')\left.\frac{\partial V_{\mathrm{XC}}}{\partial n}\right|_{n(\bar{r})}. \tag{6}$$

The integral Equation (5) is solved with respect to Φ^{SCF}: representing the equation with the same B-spline basis set leads to the solution of a linear system of algebraic equations. An efficient way to implement the construction of the χ matrix in the present B-spline basis set has been described recently [10].

Once Φ^{SCF} is obtained, all the parameters which describe the photoionization process at the TDDFT level of theory and within the dipole approximation, namely the cross section and the asymmetry parameters, are calculated via transition moments using Φ^{SCF} instead of the pure dipole operator.

3 Photoelectron angular distribution

The basic assumption in the application of angle-resolved photoelectron spectroscopy is the dipole approximation (DA) for photon–matter interaction. The DA leads to a well-characterized and easily quantified behavior of the cross section, $\mathrm{d}\sigma/\mathrm{d}\Omega$, as a function of the ejection angle θ of the photoelectron with respect to the axis of polarization of the incident radiation. In case of fully linear polarization of light, $\mathrm{d}\sigma/\mathrm{d}\Omega$ is given by

$$\frac{\mathrm{d}\sigma}{\mathrm{d}\Omega} = \frac{\sigma}{4\pi}\left[1 + \beta P_2(\cos\theta)\right] \tag{7}$$

where β is the dipolar asymmetry parameter. The application of the DA to the angular distributions of photoelectrons has provided useful information on the photoionization process itself and the orbital structure of the molecular targets [35].

3.1 Dichroism in photoionization of chiral molecules

Even within DA, it can be shown in general that the differential cross section expression (Eq. 7) can be extended to the case of circularly polarized light and of randomly oriented chiral molecular targets. The following expression holds in terms of three quantities, namely, the cross section σ, the asymmetry parameter β and the

dichroism parameter D:

$$\frac{d\sigma}{d\Omega} = \frac{\sigma}{4\pi}\left[1 + \left(-1/2\right)^{|m_r|}\beta P_2(\cos\theta) + m_r D P_1(\cos\theta)\right] \quad (8)$$

where m_r is 0, +1 or −1, respectively for linear, left circular or right circular polarization. Moreover, the D parameter is always zero unless the molecule is chiral. The laboratory frame is defined by the incident photons: the polar axis corresponds to the electric vector or propagation direction respectively for linear or circular light polarization. The cross section, the asymmetry and dichroism parameters profiles for randomly oriented molecules can be conveniently computed according to the angular momentum transfer formalism [19,36] in terms of electric-dipole matrix elements between final continuum and bound initial states.

3.2 Beyond the dipole approximation

While it is well known that DA breaks down in the hard-X-ray range [37], in the UV and X-UV photon-energy ranges, DA is assumed to hold because relativistic effects can be neglected and the wavelength of the incident radiation is much larger than the size of the electron orbits. Therefore, the effects due to interactions beyond the DA in the intermediate soft X-ray photon-energy range have been neglected for a long time. Recent measurements in noble gases provided evidences of the breakdown of the DA already in the VUV region of the spectrum with departure from the DA observed for photon energies as low as few tens of eV [38 and references therein]. In the soft-X-ray domain, a first order correction to the DA in photon momentum, which takes into account the electric–dipole electric–quadrupole and electric–dipole magnetic–dipole cross terms, is usually sufficient to properly describe $d\sigma/d\Omega$ [38]. In this approximation and for achiral systems, $d\sigma/d\Omega$ additionally depends on two new parameters, δ and γ, and on the azimutal angle ϕ relative to the photon propagation vector [38],

$$\frac{d\sigma}{d\Omega} = \frac{\sigma}{4\pi}\left\{1 + \beta P_2(\cos\theta) + \left[\delta + \gamma\cos^2\theta\right]\sin\theta\cos\phi\right\} \quad (9)$$

for pure linearly polarized light along the Laboratory Frame (LF) $\hat{Z}$ axis, and

$$\frac{d\sigma}{d\Omega} = \frac{\sigma}{4\pi}\left\{1 - \frac{\beta}{2}P_2(\cos\theta) + \left[\frac{\gamma}{2}\mathrm{sen}^2\theta + \delta\right]\cos\theta\right\} \quad (10)$$

for circularly polarized light propagating along the LF $\hat{Z}$ axis. Here, θ and ϕ denote the polar angles of the photoelectron momentum vector $\mathbf{k}$ in the LF, the positive $\hat{X}$ axis being defined by the photon propagation vector for linearly polarized light. Non-dipolar effects manifest themselves through backward/forward anisotropies along the photon momentum. These can be forward directed, for positive values of γ and δ, or backward directed for negative values of the parameters. General expressions for the non-dipole parameters δ and γ of Eqs. (9) and (10) in terms of electric/magnetic–dipole and electric–quadrupole matrix elements between final continuum and bound initial states are given in Ref. [39]. Chirality of the molecular system further introduces additional parameters [40].

4 Applications

4.1 TDDFT photoionization of SF_6

The calculations have been performed at the TDDFT level employing the non-iterative algorithm (Eq. 5) and working with the multicentric B-spline basis set (LCAO) [11].

In Fig. 1, the cross section and the asymmetry parameter profiles of the three outermost molecular orbitals of SF_6 are considered. For each ionization, three theoretical curves are plotted: the TDDFT obtained with both LB94 and SAOP potentials, in order to assess the performances with respect to the experiment, and the KS LB94, useful to identify the role of response effects and interchannel coupling, not included at the KS level, in comparison with the TDDFT results. The experimental data reported in the figures have been taken from Ref. [41], the latter being the most recent and complete experimental work.

The calculated TDDFT profiles are generally always in very good agreement with the experimental data, and the SAOP potential performs better than the LB94 one. The differences between the KS and the TDDFT results are not so large, apart from the region just above the threshold dominated by autoionization resonances, which cannot be calculated at the simpler KS level. An interesting exception is the C ^2E_g ionization, where in both cross section and asymmetry parameter profiles, the TDDFT definitely improves the agreement with respect to the experiment in a wide energy range from threshold up to 10 eV above it. Given the excellent agreement between theory and experiment, the present TDDFT method is suitable to give a reliable interpretation and therefore to propose assignments of the observed spectral features. In particular, SF_6 cross section profiles display several shape resonances assuming very different appearance: for example, in X $^2T_{1g}$ profile a wide and smooth maximum is observed, while in (A, B, $^2T_{1u}$, $^2T_{2u}$) two very sharp structures are observed.

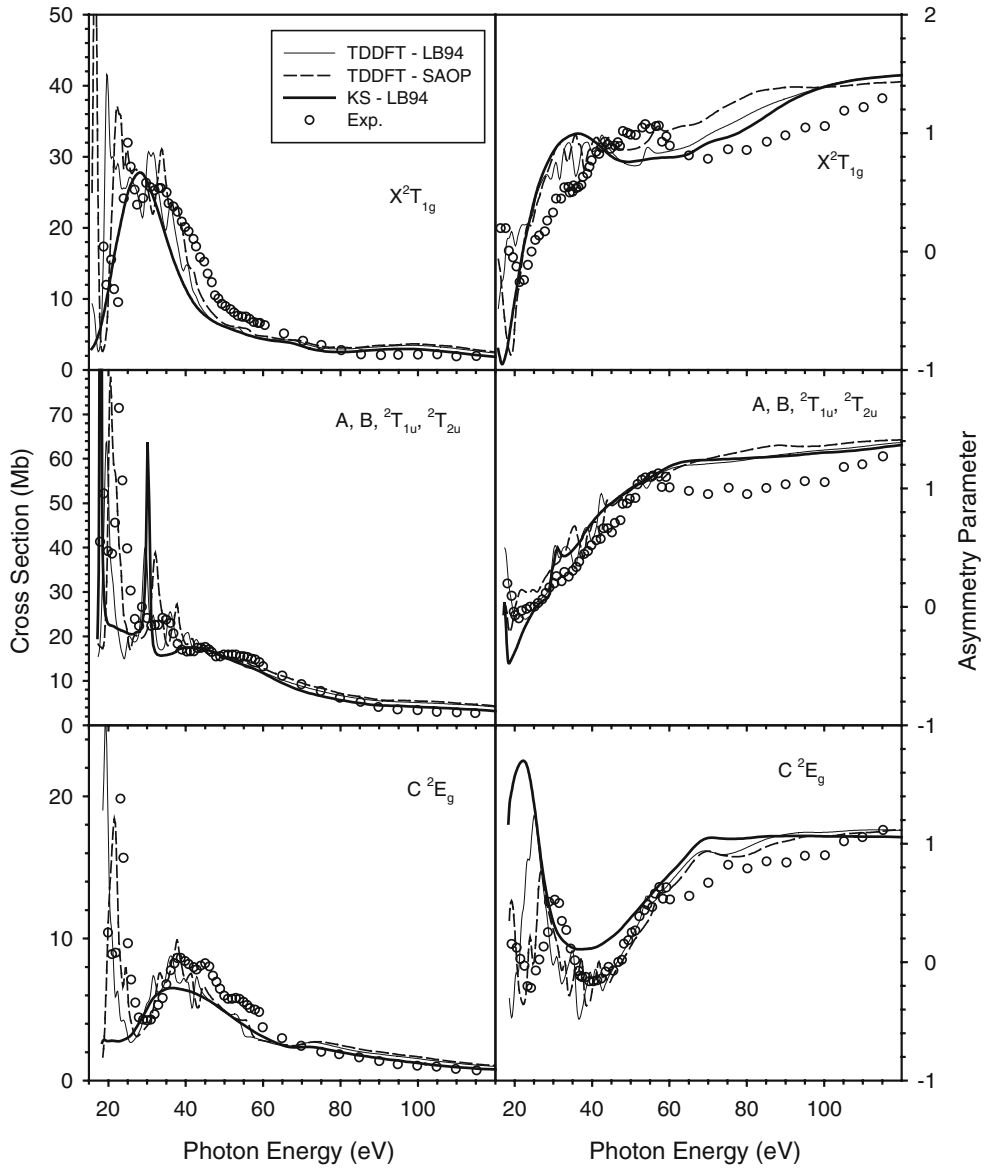

Fig. 1 Cross section (*left panels*) and asymmetry parameter (*right panels*) profiles, relative to the X, the A, B and the C photoelectron bands of SF_6. Experimental data from Ref. [41]

The presence of such shape resonances is known since long ago [42] and represents one of the most interesting peculiarities in the photoionization of SF_6. In the (A, B, $^2T_{1u}$, $^2T_{2u}$) profile, passing from KS-LB94 to the TDDFT–LB94 profile, one observes a slight shift of the first resonance to higher energy, while the second one remains roughly at the same energy position. A further shift to higher energy of both shape resonances is obtained at the TDDFT–SAOP level. From symmetry resolved cross section analysis, it is possible to ascribe the first resonance at 0.76 eV to the $5t_{1u} \rightarrow \varepsilon t_{2g}$ continuum, while the second one at 12.20 eV is attributed to the $5t_{1u} \rightarrow \varepsilon e_g$ continuum, in line with previous assignment [41]. In order to give a more physical interpretation of the shape resonances, we have also performed an analysis of the shape resonances based on the "dipole prepared" continuum orbitals [43], which allow the analysis of the photoelectron wave function removing the problem of the infinite continuum degeneracy. We have reported the plots relative to the εt_{2g} and εe_g resonances in the two upper panels of Fig. 2: as can be easily seen, while the first resonance at 0.76 eV corresponds to a continuum orbital with a strong S3d character with lobes directed away from the F atoms, the resonance state at 12.20 eV keeps the S3d character, but with lobes directed towards the F atoms and strong antibonding interaction of type σ^*(S–F). This analysis confirms the common interpretation of these shape resonances in terms of

continuum quasi-bound states, trapped inside the molecular cage by the double well-effective potential generated by the electronegative fluorine atoms. The εe_g resonance lies at more than 10 eV higher than the εt_{2g} one because of the strong antibonding interaction with the ligands. Moreover, they are both very sharp indicating that the trapping of the d-wave inside the cage is effective only in a very limited region of photoelectron energies. It is convenient to compare the resonance plots with respect to the continuum orbitals taken few eV's away from the resonances, as reported in the two central panels of Fig. 2: in this case the wave function is much weaker inside the cage, but it also completely loses its structure, which on the resonance is caused by the anisotropic molecular effective potential and outside the resonance shows an almost perfect spherical shape. These findings corroborate the idea that such shape resonances are greatly enhanced and sharpened as an effect of the anisotropic molecular effective potential.

It is interesting to compare these findings with the behavior of the HOMO $1t_{1g}$ cross section, which displays an intense maximum at 12.9 eV of photoelectron kinetic energy, and is ascribed to the $1t_{1g} \rightarrow \varepsilon t_{2u}$ continuum. The latter is found to be much broader than those attributed to the $5t_{1u} \rightarrow \varepsilon t_{2g}$ and $5t_{1u} \rightarrow \varepsilon e_g$ shape resonances. In Fig. 2, we have also reported the "dipole prepared" continuum orbital for the $1t_{1g} \rightarrow \varepsilon t_{2u}$ continuum (lower panel), which can be ascribed to a wave of the $f_{(x^2-y^2)z}$ type. A possible interpretation of such different resonant behavior could be that in $1t_{1g} \rightarrow \varepsilon t_{2u}$ continuum resonance, the maximum of the cross section is caused by a potential barrier that originates from the centrifugal term associated with the high angular momentum ($l = 3$) of the photoelectron. This barrier is spherically symmetric and prevents the photoelectron from penetrating into the molecular cage, originating a delayed onset at higher photoelectron energy. In summary, we suggest that the different observed shape resonance behaviors originate from the nature of the barrier in the potential: spherical barriers associated with the centrifugal kinetic energy term give rise to broad resonances characterized by a high angular momentum of the photoelectron, while non-spherical barriers associated with ligand repulsive terms give rise to sharp resonances.

4.2 Dichroism in photoionization of chiral molecules

Continuum calculations on chiral molecules is a challenge, due to the large size and low symmetry of the systems considered. To this end, we employ a KS formalism with a B-spline LCAO basis, a convenient scheme that is however still very demanding in terms of computational power due to the large matrices involved in the calculations. In order to tackle this task, we have parallelized our KS–LCAO code with standard MPI libraries to fully exploit the architectures of modern distributed memory supercomputers.

The first studied system has been the methyl-oxirane for which new experimental data were available for comparison, thus providing a stringent test for the accuracy of the theory [19,44]. Furthermore, this molecule presents a high degree of conformational rigidity that makes it suitable for extensive calculations and avoids an equilibrium mixture of conformers to contribute to the measured dichroism. For a correct assessment of the dynamics of the CDAD effect, it is much more informative to analyze the D parameter for each orbital as a function of the photoelectron energy, rather than to consider the D parameter as a function of the binding energy as in the dichroic spectrum. The theoretical dichroism coefficient has been therefore calculated as a function of the photon energy for the valence photoionization channels and compared with the experimental measurements (Fig. 3). It is apparent that the magnitude and sign of the theoretical and experimental D coefficients are in good agreement. This first study clearly indicates that the $D_i(\omega)$ coefficient exhibits a rich dynamical behavior and is a promising tool to investigate molecular dissymmetry. The D parameter appears quite sensitive to the nature of the ionized orbital and therefore could be profitably employed to probe chiral molecules and extract useful information on their electronic structure. A main task is the correlation between the shapes of the D parameters with the electronic structure of the system, or more precisely the identification of the physical origin of the different patterns observed in the D profiles. This task, however, is still challenging: in fact, the numerical value of the $D_i(\omega)$ is the resultant of many contributions [19], and it is very difficult to identify a simple cause. More experimental and theoretical work on a larger variety of molecules are necessary to gain more insight into this relationship; to this purpose, a series of derivatives of oxirane has been considered (see Scheme 1) [23]. Despite the lack of experimental data (except for I), these molecules have been chosen because the F atom is the simplest electronegative electron-acceptor substituent, which may represent a useful model to mimic real, but more complex, chiral molecules, in order to identify the relations between the CDAD and the molecular electronic structure. In particular, the dichroic parameter profiles relative to the valence orbitals have been studied for the states that retain their nature along the series. For example, Fig. 4 reports the D parameter profile of the MOs corresponding to the oxygen lone pair of the four molecules. Such

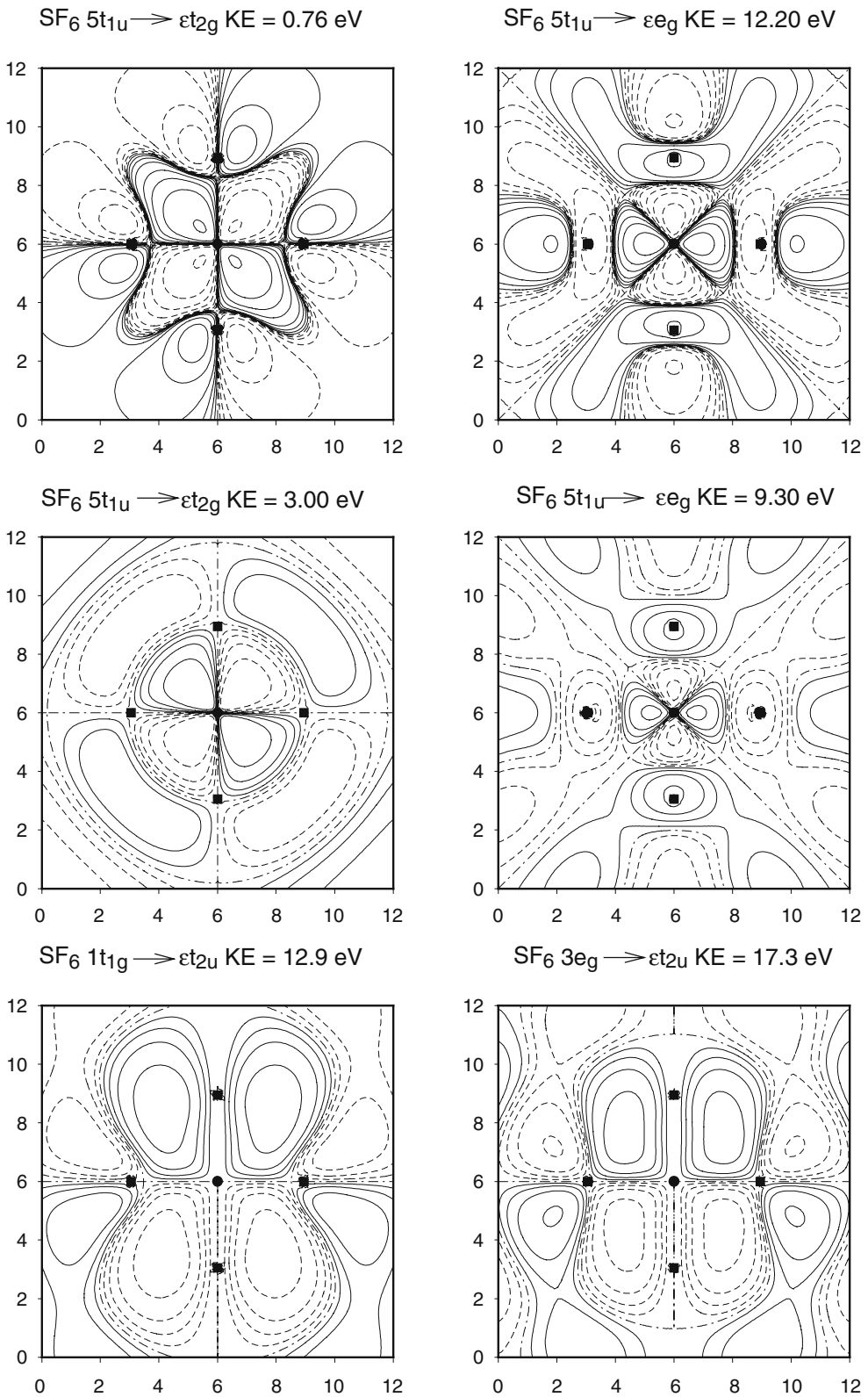

Fig. 2 Contour plots over the plane containing the S atom and four F atoms of the "dipole prepared" continuum orbitals at the given photoelectron kinetic energy for SF_6. Positive, negative and zero (nodal) isolines are represented by *solid*, *dashed* and *dot-dashed lines*, respectively. S and F atoms positions are shown as *filled circles* and *squares*, respectively. Scale in atomic units (Bohr)

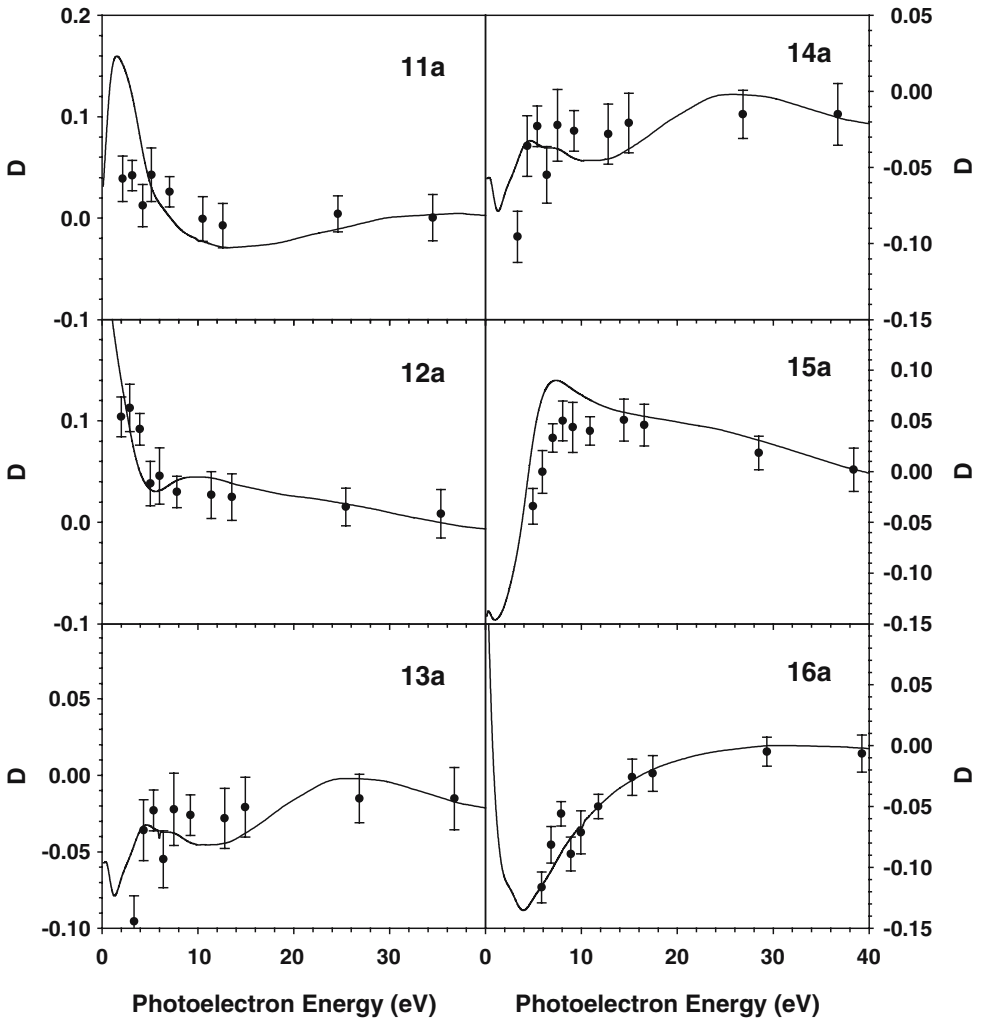

Fig. 3 Calculated (*solid line*) and experimental (*full circles with error bars*) [44] dichroism parameter D of S-methyloxirane relative to the 11a–16a molecular orbitals

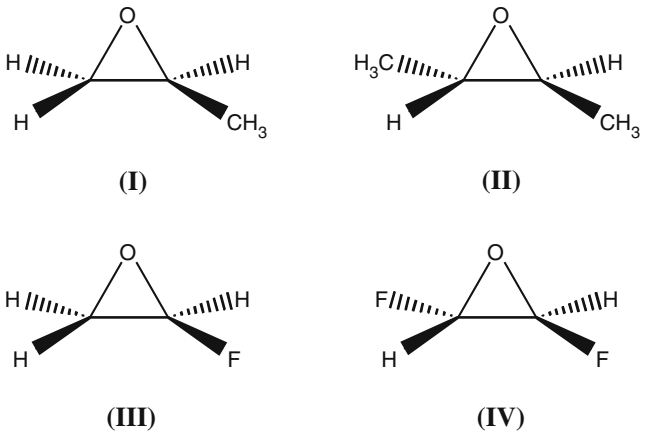

Scheme 1 Structures of the chiral molecules considered in this study: **(I)** (S)-methyloxirane; **(II)** *trans*-(2S,3S)-dimethyloxirane; **(III)** (S)-fluoroxirane; **(IV)** *trans*-(2S,3S)-difluoroxirane

comparison is meaningful because we have checked that in all cases the oxygen lone pair keeps its nature along the series. The theoretical results show two interesting features: first, the significant oscillation of the D values (of the order of 20% in terms of relative intensity), which should be experimentally detectable. Second, the D parameter proves to be very sensitive to the chemical substitution of the oxirane ring. In particular, the shift to higher energy of the profile in (II) with respect to (I) is ascribed to the electronic effect of the increasing number of methyl groups, which acting as electron donors, increase the electron density on the O atom. Furthermore, the large negative values calculated for the D parameter in (IV) can be associated with the electronegative effect of the F substitution, which gradually competes with that of the O atom, on going from (III) to (IV)

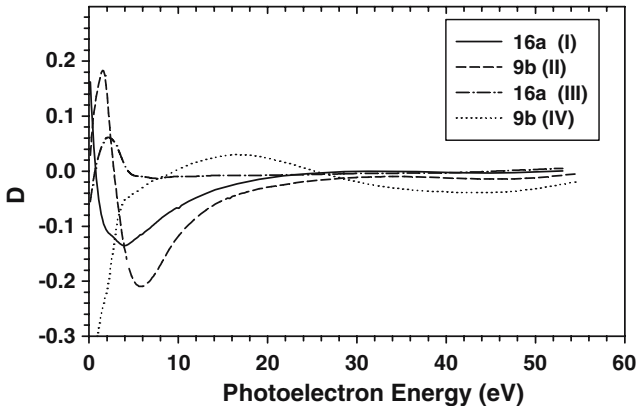

Fig. 4 Dichroic parameter (D) relative to the 16a **(I)**, 9b **(II)**, 16a **(III)** and 9b **(IV)**orbitals and molecules respectively (see Scheme 1)

molecules. Also the core dichroism has been considered relative to the O 1s and C 1s orbitals of these molecules (Fig. 5). It can be observed that for core ionizations the CDAD effect is less intense than in the valence shell; furthermore the chiral center is not necessarily connected with the most pronounced dichroism. This finding indicates that for the core states, the dichroism must be a final state effect; in fact the initial state core orbitals retain their atomic spherical symmetry, therefore the dichroism is ascribed to the photoelectron wave function which is delocalized and can probe the whole effective molecular potential, extracting information on its dissymmetry.

The study of the dichroism effects appears particularly significant in biological systems; in this respect, the camphor molecule is an excellent candidate to be studied because of its rigidity [45]. Furthermore, measurements of photoelectron dichroism are reported in the literature for both the core [46] and the outer valence [17,18] regions, allowing comparison with the theoretical results. The calculated dichroic parameters for the carbonyl core C 1s and O 1s ionizations (Fig. 6) show rather large variations at low kinetic energies; this finding is significant because of the high localization of the 1s initial core orbital, which is not asymmetric, as pointed before. This confirms that the dichroism cannot be simply associated with the chirality of the initial state but rather with the continuum final state, which is completely delocalized over the molecule and is therefore able to sample the asymmetry of the effective potential. The significant differences in the dichroic parameters relative to the two C 1s and O 1s core orbitals (opposite sign and different shape) indicate the sensitivity of the D parameter to the chemical environment of the atom, as already found in the series of analogue compounds [23]. As concerns the valence ionization, the

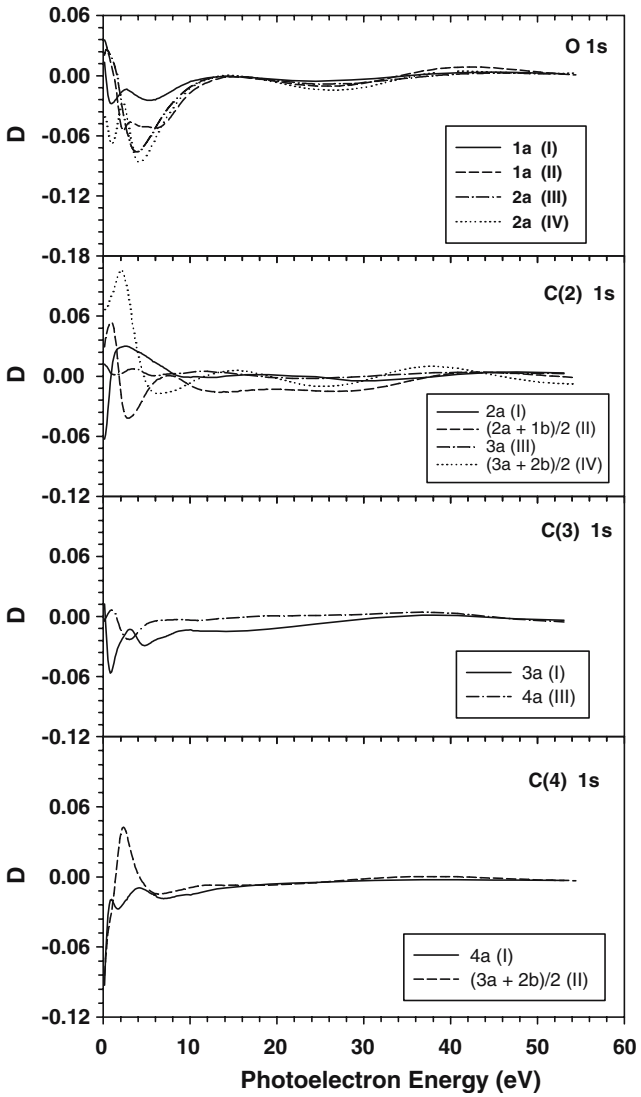

Fig. 5 Dichroic parameter (D) relative to the O 1s, C(2) 1s, C(3) 1s and C(4) 1s core orbitals of oxirane derivatives (see Scheme 1)

dichroic parameter has been evaluated for the outermost orbital (HOMO), which can be characterized as the carbonyl oxygen lone pair. The comparison with the experiment is reported in Fig. 7 and some discrepancies are revealed, in particular, the energy gap calculated between the maximum and the minimum is too narrow. A non-completely quantitative agreement can be ascribed to a limitation of the DFT KS Hamiltonian employed in the calculations; the inclusion of response effects through the TD-DFT approach would possibly improve the agreement, as it has been shown for the calculation of photoionization parameters in small molecules [5–7].

The theoretical studies on methyloxirane and camphor molecules [19,23,45] make the assumption that in the calculation of the CDAD effect, the rotation of the

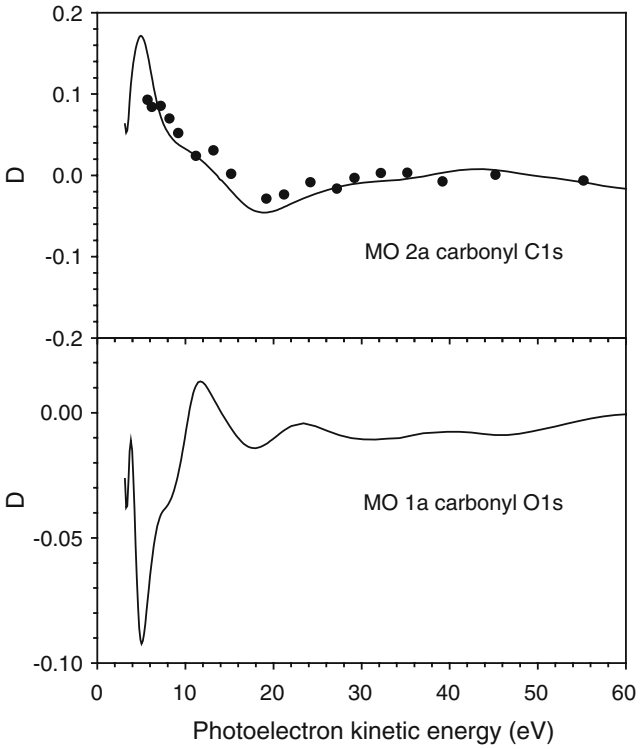

Fig. 6 Dichroic parameter (D) relative to the camphor 2a (carbonyl C1s) and 1a (carbonyl O1s) orbitals. *Solid line* B-spline LCAO DFT calculation, *symbols* are experimental data from Ref. [46]

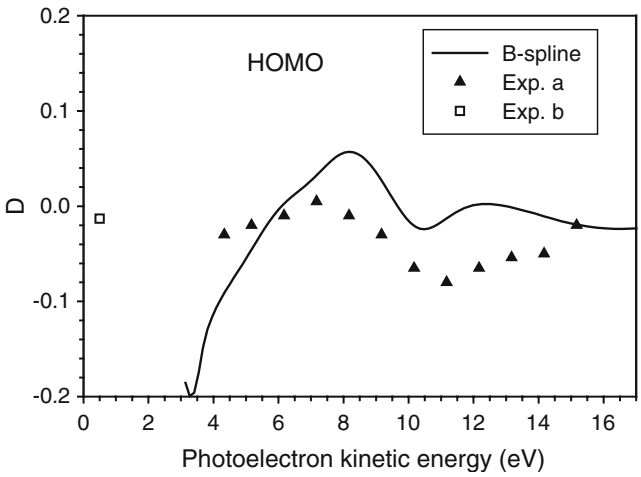

Fig. 7 Dichroic parameter (D) relative to the camphor HOMO orbital. *Solid line* B-spline LCAO DFT calculation, *symbols* are experimental data, **a** Ref. 18, **b** Ref. [17]

methyl group does not affect the results. However, it is an interesting question if circular dichroism in photoemission could be used as a practical tool for confomational analysis, as it occurs in conventional circular dichroism in differential absorption. The sensitivity of the CDAD to the conformation of the

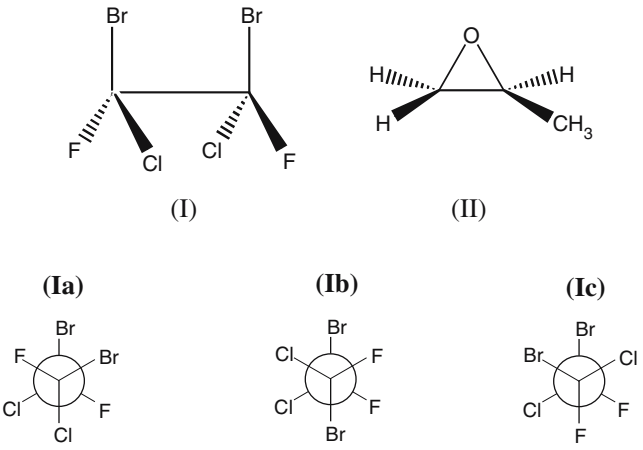

Scheme 2 Configurational structures of the molecules: **(I)** (1R,2R)-1,2-dibromo-1,2-dichloro-1,2-difluoroethane; **(II)** (S)-methyloxirane; and the three conformers Ia Ib and Ic of (I)

molecule has been analyzed in Ref. [47] with reference to the (1R,2R)-1,2-dibromo-1,2-dichloro-1,2-difluoroethane (see Scheme 2, I), whose possible conformations derive from the C–C bond rotation (three conformational isomers Ia, Ib and Ic are stable at room temperature). CDAD calculations on the possible conformers of (S)-methyloxirane (II), as obtained from internal rotation about the C–CH_3 bond, have been also considered in that study [47]. Another unexpected and dramatic sensitivity of the dichroic parameter profile to the methyl rotation, both in the core and valence region, has been found. It is of worth to note that the other photoionization dynamical parameters, namely the cross section and the asymmetry parameter, are instead only weakly affected. Figure 8 reports some of the results relative to both the core and valence dichroism of the three conformers of I. The D parameter for the core orbitals (F 1s and C 1s) shows high sensitivity to the conformational changes, particularly near the threshold. The core states maintain their IP position along the conformers very well and the D profiles can therefore be proposed as a useful tool for conformational analysis and possibly employed as "fingerprint" of the different conformers of a molecule. A rather large CDAD effect is also detected for the HOMO ionization, whose orbital has a localized character too, being essentially composed of Br 4p functions. These observations indicate that the sensitivity of the D parameter to the particular conformer should be ascribed to the continuum final state, which feels the changes of the effective molecular potential during the C–C rotation. This is in agreement with the results previously discussed and confirms that the CDAD effect appears more strongly affected by the particular molecular structure than the initial state. Another recent computational and experimental study on the circular dichroism

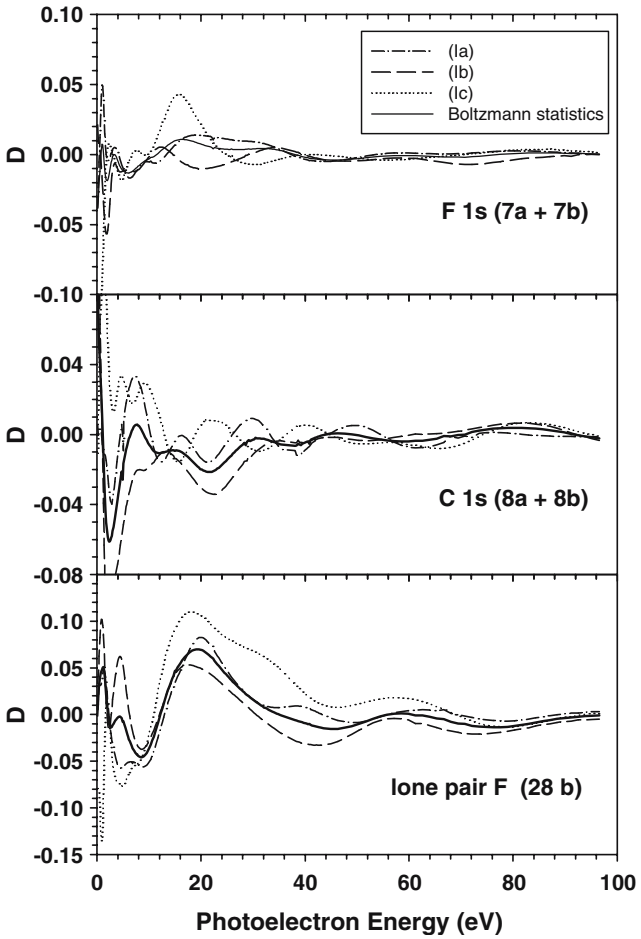

Fig. 8 Dichroic parameter (D) relative to the total core F 1s (7a + 7b), C 1s (8a + 8b) and valence 28b (lone pair of fluorine atoms) orbitals of the conformers of (1R,2R)-1,2-dibromo-1,2-dichloro-1,2-difluoroethane **(I)** (See Scheme 2). The averaged D values obtained on the basis of the Boltzmann's statistics are also displayed

in the valence region of the 3-hydroxytetrahydrofuran enantiomers [20] also demonstrates the sensitivity of the dichroic parameter to conformational factors.

4.3 Photoionization beyond the dipole approximation

The calculation of non-dipolar terms has been implemented by now at the KS level, with an LCAO B-spline basis set. As an example of the performance of our method in calculating nondipole angular distribution parameters, we consider the K-shell ionization of molecular nitrogen [39] for which experimental and theoretical calculations from different sources are available [24–26]. There have been two independent measurements of non-dipolar angular distributions giving contradicting conclusions. The experimental work by Hemmers et al. [25] revealed a resonant behavior in the ζ parameter (defined as $\zeta = \gamma + 3\delta$) with a peak energy position of about 60 eV above threshold. The peak energy position of the feature in the ζ profile is therefore difficult to correlate with the well-known σ^* shape-resonance in the $1\sigma_g^{-1}$ cross section [48]. Recent measurements [26] do not support these findings however, and negligible deviations from the dipole distributions in the near threshold region are found. We report our DFT results in Fig. 9, and make a comparison with the experimental β measurements [24,26,49] and the two sets of experimental data for the non-dipole parameters [25,26]. We report the DFT results resolved in the core-ion states ($1\sigma_g^{-1}$ and $1\sigma_u^{-1}$ ionization channels), as well as their average, weighted by the corresponding partial cross sections. Our results are fully consistent with the experimental results of Ref. [26]; DFT results for the γ parameter are in very good agreement with the experimental values of Ref. [26] and discrepancies with our predictions for δ fall within the experimental uncertainties. Strong near-threshold deviations from the DA are predicted for the individual $1\sigma_g^{-1}$ and $1\sigma_u^{-1}$ ionization channels, in good agreement with the Random Phase Approximation (RPA) results of Ref. [26], but almost complete cancellation occurs in the average values, which display smooth and monotonic variations in the whole spectral range, resembling the atomic case [24]. This is a good example of coherent electron emission from two identical sites, whose quantum coherence is obscured with experiments that do not resolve the individual quantum (gerade and ungerade) states [50]. Our DFT results are in rather good agreement with the RPA predictions of Ref. [26] (not reported in the Figure for the sake of clarity), with the only exceptions of a near threshold oscillation in the δ parameter, which is absent in our results, and a small shift of the RPA γ profiles for the individual $1\sigma_g^{-1}$ and $1\sigma_u^{-1}$ ionization channels toward higher excitation energies when compared to our results, due to a different attractive character in the effective KS and RPA scattering potentials. The statement that non-dipole effects prove negligible for nitrogen K-shell photoionization in the near-threshold range is therefore putforth on a firm basis because results from two different theoretical approaches are in satisfactory agreement with each other and with the new experimental data of Hosaka et al. [26]. The extent of the agreement between our theoretical results and the RPA ones of Ref. [26] furthermore suggests that interchannel coupling effects between main-line $1\sigma_g^{-1}$ and $1\sigma_u^{-1}$ ionization channels prove quite unimportant in determining deviations from the dipolar angular distribution and further that relaxation effects are phenomenologically rather well accounted for by the LB94 xc potential [51].

We now analyze the high energy behavior of the various asymmetry parameters. The individual $1\sigma_g^{-1}$ and $1\sigma_u^{-1}$ asymmetry parameters are seen to oscillate out of phase; the oscillations are characterized by a rather small amplitude in the β parameter but persist without damping in the γ and δ profiles. The out of phase oscillations originate from the different parities of the initial states, and consequently, of the continuum partial waves, and this, as stressed above, leads to cancellations in the averaged values. This strong oscillatory character furnishes a nice proof of the validity of the Cohen–Fano model [52], which is then invoked for its explanation. In fact, consider in Fig. 9 the crossing points of the γ parameters for the $1\sigma_g^{-1}$ and $1\sigma_u^{-1}$ states: they occur approximately in steps of 1.5 a.u. of photelectron momentum. Then, assuming a sin (kR) dependence as implied by the

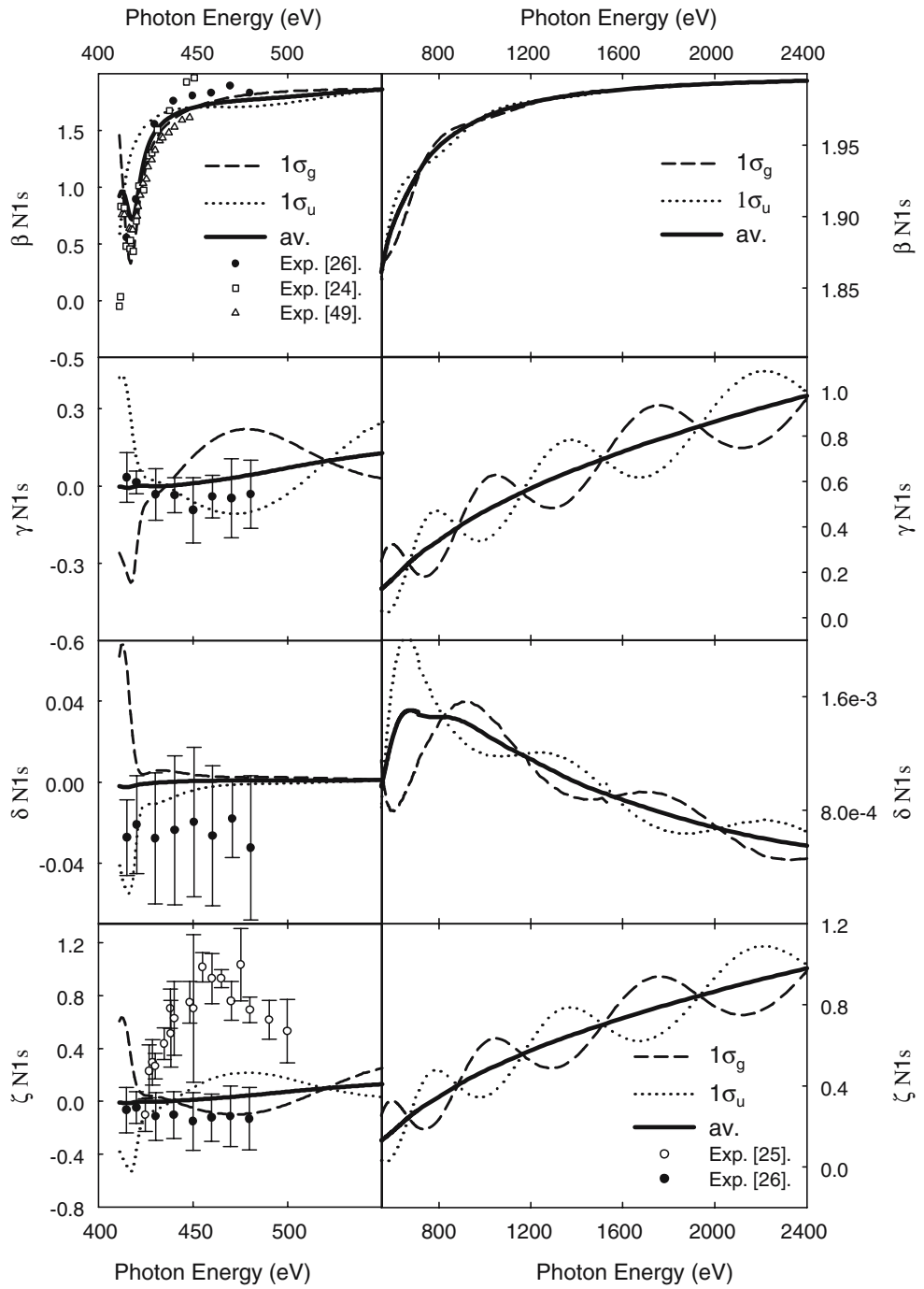

Fig. 9 Calculated and experimental asymmetry and non-dipolar parameters of N_2

Cohen–Fano model, we arrive at a distance R of 2.09 a.u. in good agreement with the equilibrium distance of 2.07 a.u. used as input in our fixed-nuclei calculations, and with the results of a similar analysis presented by Hosaka et al. [26].

In summary, our DFT results agree reasonably well with the recent RPA calculations and with the available experimental data in the near threshold range. The KS results are fully consistent with the most recent theoretical and experimental findings [26] and rather small non-dipole effects are found in the near threshold range. However non-dipole terms turn out to be quite large, even at the threshold, when individual contributions from the $1\sigma_g^{-1}$ and $1\sigma_u^{-1}$ ionization channels are considered. Interference effects giving rise to high-energy oscillations in the dipole and non-dipole asymmetry parameters are analyzed and explained in the framework of the Cohen–Fano model. Efforts are currently on for the inclusion of dynamical correlation effects in the framework of the linear response theory (TDDFT).

5 Conclusions

From the methodological point of view, the formalism of the TDDFT applied to molecular continuum, with a new implementation based on a non-iterative algorithm and a multicentric B-spline basis, has proved quite successful for a quantitative description of the photoionization dynamics for medium sized molecules. Extensions of the KS method for the calculations of photoionization dynamical parameters beyond the dipole approximation have been considered and implemented at the LCAO level, while the calculation of dichroism of photoelectrons of chiral molecules within the dipole approximation has been implemented in a multicentric basis and the codes have been parallelized. The methods have proved successful to accurately reproduce experimental data and to suggest reliable assignments of the observed spectral features. Future extensions regard the implementation of the non-dipolar terms at the TDDFT level of the theory and the parallelization of the TDDFT code to extend the range of applicability to larger and less symmetric systems.

Acknowledgments This work has been supported by grants from MIUR (Programmi di Ricerca di Interesse Nazionale COFIN 2004 and FIRB 2001) of Italy, from Consorzio Interuniversitario Nazionale per la Scienza e Tecnologia dei Materiali (INSTM) (Progetto PRISMA 2004) and CNR of Rome (Italy). D. T also acknowledges CNR-INFM DEMOCRITOS (Istituto Nazionale di Fisica della Materia) for a postdoctoral fellowship.

References

1. Kohn W, Sham LJ (1965) Phys Rev 140:A1133
2. Bachau H, Cormier E, Decleva P, Hansen JE, Martín F (2001) Rep Prog Phys 64:1601
3. Casida ME (1996) In: Recent developments and applications of modern density functional theory, Seminario JM (ed), Theoretical and Computational Chemistry vol 4. Elsevier, Amsterdam, p 391
4. van Gisbergen SJA, Snijders JG, Baerends EJ (1995) J Chem Phys 103:9347
5. Stener M, Decleva P (2000) J Chem Phys 112:10871
6. Stener M, Fronzoni G, Toffoli D, Decleva P (2002) Chem Phys 282:337
7. Fronzoni G, Stener M, Decleva P (2003) J Chem Phys 118:10051
8. Stener M, Decleva P, Cacelli I, Moccia R, Montuoro R (2001) Chem Phys 272:15
9. Fronzoni G, Stener M, Decleva P (2004) Chem Phys 298: 141–153
10. Stener M, Fronzoni G, Decleva P (2005) J Chem Phys 122(1–11):234301
11. Stener M, Toffoli D, Fronzoni G, Decleva P (2006) J Chem Phys 124:114306
12. Toffoli D, Stener M, Decleva P (2006) Phys Rev A 73:042704
13. Toffoli D, Stener M, Fronzoni G, Decleva P (2006) J Chem Phys 124:214313
14. Ritchie B (1976) Phys Rev A 13:1411
15. Cherepkov NA (1982) Chem Phys Lett 87:344
16. Bowering N, Lischke T, Schmidtke B, Muller N, Khali T, Heinzmann U (2001) Phys Rev Lett 86:1187
17. Garcia G, Nahon L, Lebech M, Houver JC, Dowek D, Powis I (2003) J Chem Phys 119:8781
18. Litschke T, Böwering N, Schmidtke B, Müller N, Khalil T, Heinzmann U (2004) Phys Rev A 70:22507
19. Turchini S, Zema N, Contini G, Alberti G, Alagia M, Stranges S, Fronzoni G, Stener M, Decleva P, Prosperi T (2004) Phys Rev A 70:014502–1
20. Giardini A, Catone D, Stranges S, Satta M, Tacconi M, Piccirillo S, Turchini S, Zema N, Contini G, Prosperi T, Decleva P, Di Tommaso D, Fronzoni G, Stener M, Filippi A, Speranza M (2005) Chem Phys Chem 6:1164
21. Powis I (2000) J Chem Phys 112:301
22. Powis I (2000) J Phys Chem A 104:878
23. Stener M, Fronzoni G, Di Tommaso D, Decleva P (2004) J Chem Phys 120:3284
24. Langhoff PW, Arce JC, Sheehy JA, Hemmers O, Wang H, Focke P, Sellin IA, Lindle DW (2001) J Electron Spectrosc Relat Phenom 114–116:23
25. Hemmers O, Wang H, Focke P, Sellin IA, Lindle DW, Arce JC, Sheehy JA, Langhoff PW (2001) Phys Rev Lett 87:273003
26. Hosaka K, Adachi J, Golovin AV, Takahashi M, Teramoto T, Watanabe N, Yagishita A, Semenov SK, Cherepkov NA (2006) J Phys B: At Mol Opt Phys 39:L25
27. Baerends EJ, Ellis DE, Ros P (1973) Chem Phys 2:41
28. Fonseca Guerra C, Snijders JG, te Velde G, Baerends EJ (1998) Theor Chem Acc 99:391
29. Van Leeuwen R, Baerends EJ (1994) Phys Rev A 49:2421
30. Schipper PRT, Gritsenko OV, van Gisbergen SJA, Baerends EJ (2000) J Chem Phys 112:1344
31. Venuti M, Stener M, Decleva P (1998) Chem Phys 234:95
32. Toffoli D, Stener M, Fronzoni G, Decleva P (2002) Chem Phys 276:25
33. Zangwill A, Soven P (1980) Phys Rev A 21:1561
34. Gross E, Kohn W (1990) Adv Quantum Chem 21:255
35. Green JC, Decleva P (2005) Coord Chem Rev 249:209

36. Chandra N (1987) J Phys B 20:3405
37. Tseng HK, Pratt RH, Yu S, Ron A (1978) Phys Rev A 17:1061
38. Hemmers O, Guillemin R, Lindle DW (2004) Rad Phys and Chem 70:123
39. Toffoli D, Decleva P (2006) J Phys B: At Mol Opt Phys 39:2681
40. Grum-Grzhimailo AN (2003) J Phys B: At Mol Opt Phys 36:2385
41. Holland DMP, MacDonald MA, Baltzer P, Karlsson L, Lundqvist M, Wannberg B, von Niessen W (1995) Chem Phys 192:333
42. Dehmer JL, Parr AC, Wallace S, Dill D (1982) Phys Rev A 26:3283
43. Fronzoni G, Stener M, Furlan S, Decleva P (2001) Chem Phys 273:117
44. Stranges S, Turchini S, Alagia M, Alberti G, Contini G, Decleva P, Fronzoni G, Stener M, Zema N, Prosperi T (2005) J Chem Phys 122:244303
45. Stener M, Di Tommaso D, Fronzoni G, Decleva P, Powis I (2006) J Chem Phys 124:024236
46. Hergenham U, Rennie EE, Kugeler O, Marburger S, Lischke T, Powis I, Garcia G (2004) J Chem Phys 120:4553
47. Di Tommaso D, Stener M, Fronzoni G, Decleva P (2006) Chem Phys Chem 7:924
48. Hergenhahn U, Kugeler O, Rüdel A, Rennie EE, Bradshaw AM (2001) J Phys Chem A 105:5704
49. Kempgens B, Kivimäki A, Neeb M, Köppe HM, Bradshaw AM Feldhaus J (1996) J Phys B: At Mol Opt Phys 29:5389
50. Rolles D, Braune M, Cvejanovic S, Gessner O, Hentges R, Korica S, Langer B, Lishke T, Prumper G, Reinkoster A, Viefhaus J, Zimmermann BR, McKoy V, Becker U (2005) Nature 437:711
51. Stener M, Fronzoni G, Decleva P (2002) Chem Phys Lett 351:469
52. Cohen HD, Fano U (1996) Phys Rev 150:30